

Hemodynamic Deconvolution Demystified: Sparsity-Driven Regularization at Work

Eneko Uruñuela^{a,b,*}, Thomas A.W. Bolton^{c,d}, Younes Farouj^d, Dimitri Van De Ville^{d,e}, César Caballero-Gaudes^a

^a*Basque Center on Cognition, Brain and Language (BCBL), Donostia-San Sebastián, Spain.*

^b*University of the Basque Country (EHU/UPV), Donostia-San Sebastián, Spain.*

^c*Gamma Knife Center, Department of Clinical Neuroscience, Centre Hospitalier Universitaire Vaudois (CHUV), Lausanne, Switzerland*

^d*Ecole Polytechnique Fédérale de Lausanne (EPFL), Lausanne, Switzerland.*

^e*Faculty of Medicine, University of Geneva, Geneva, Switzerland*

Abstract

Deconvolution of the hemodynamic response is an important step to access short timescales of brain activity recorded by functional magnetic resonance imaging (fMRI). Albeit conventional deconvolution algorithms have been around for a long time (e.g., Wiener deconvolution), recent state-of-the-art methods based on sparsity-pursuing regularization are attracting increasing interest to investigate brain dynamics and connectivity. This technical note revisits the main concepts underlying two main methods, Paradigm Free Mapping and Total Activation, in the most accessible way. Despite their apparent differences, these methods are theoretically equivalent as they represent the synthesis and analysis sides of the same problem. We demonstrate this equivalence in practice with their best-available implementations using both simulations, with different signal-to-noise ratios, and experimental data of motor task and resting-state fMRI. We evaluate the parameter settings that lead to equivalent results, and benchmark the computational speed of both algorithms. This note is useful for practitioners interested in having a better understanding of state-of-the-art hemodynamic deconvolution, and who want to make use of them in the most efficient implementation.

Keywords: fMRI deconvolution, paradigm free mapping, total activation, temporal regularization

1. Introduction

Functional magnetic resonance imaging (fMRI) data analysis is often directed to identify and disentangle the neural processes that occur in different brain regions during task or at rest. As the blood oxygenation level-dependent (BOLD) signal of fMRI is only a proxy for neuronal activity mediated through neurovascular coupling, an intermediate step that estimates the activity-inducing signal, at the timescale of fMRI, from the BOLD timeseries can be useful. Conventional analysis of task fMRI data relies on the general linear models (GLM) to establish statistical parametric maps of brain activity by regression of the empirical timecourses against hypothetical ones built from

*Corresponding author

Email address: e.urunuela@bcbl.eu (Eneko Uruñuela)

the knowledge of the experimental paradigm. However, timing information of the paradigm can be
10 unknown, inaccurate, or insufficient in some scenarios such as naturalistic stimuli, resting-state, or
clinically-relevant assessments.

Deconvolution and methods alike are aiming to estimate neuronal activity by undoing the blurring effect of the hemodynamic response, characterized as a hemodynamic response function (HRF). Given the inherently ill-posed nature of hemodynamic deconvolution, due to the strong temporal
15 low-pass characteristics of the HRF, the key is to introduce additional constraints in the estimation problem that are typically expressed as regularizers. For instance, the so-called Wiener deconvolution is expressing a “minimal energy” constraint on the deconvolved signal, and has been used in the framework of psychophysiological interactions analysis to compute the interaction between a seed’s activity timecourse and an experimental modulation (Glover 1999; Gitelman et al. 2003;
20 Gerchen et al. 2014; Di and Biswal 2018; Freitas et al. 2020). Complementarily, the interest in deconvolution has increased to explore time-varying activity in resting-state fMRI data (Preti et al. 2017; Keilholz et al. 2017; Lurie et al. 2020; Bolton et al. 2020). In that case, the aim is to gain better insights into the neural signals that drive functional connectivity at short time scales, as well as how the spatio-temporal structure of functional components that dynamically construct
25 resting-state networks and their interactions (Karahanoglu and Ville 2017).

Deconvolution of the resting-state fMRI signal has illustrated the significance of transient, sparse spontaneous events (Petridou et al. 2012; Allan et al. 2015) that refine the hierarchical clusterization of functional networks (Karahanoglu et al. 2013) and reveal their temporal overlap based on their signal innovations not only in the human brain (Karahanoglu and Ville 2015), but also in the spinal cord (Kinany et al. 2020). Similar to task-related studies, deconvolution allows to investigate
30 modulatory interactions within and between resting-state functional networks (Di and Biswal 2013, 2015). In addition, decoding of the deconvolved spontaneous events allows to decipher the flow of spontaneous thoughts across cognitive domains while at rest (Karahanoglu and Ville 2015; Gonzalez-Castillo et al. 2019). Beyond findings on healthy subjects, deconvolution techniques have also proven
35 its utility in clinical conditions to characterize functional alterations of patients with a progressive stage of multiple sclerosis at rest (Bommarito et al. 2020), to find functional signatures of prodromal psychotic symptoms and anxiety at rest on patients suffering from schizophrenia (Zöller et al. 2019), to detect the foci of interictal events in epilepsy patients without an EEG recording (Lopes et al. 2012; Karahanoglu et al. 2013), or to study functional dissociations observed during non-rapid eye movement sleep that are associated with reduced consolidation of information and impaired consciousness (Tarun et al. 2020).

The algorithms for hemodynamic deconvolution can be classified based on the assumed hemodynamic model and the optimization problem used to estimate the neuronal-related signal. Most approaches assume a linear time-invariant model for the hemodynamic response that is inverted
45 by means of variational (regularized) least squares estimators (Glover 1999; Gitelman et al. 2003; Gaudes et al. 2010, 2012, 2013; Caballero-Gaudes et al. 2019; Hernandez-Garcia and Ulfarsson 2011; Karahanoglu et al. 2013; Cherkaoui et al. 2019; Costantini et al. 2021; Hütel et al. 2021), logistic functions (Bush and Cisler 2013; Bush et al. 2015; Loula et al. 2018), probabilistic mixture models (Pidnebesna et al. (2019)), convolutional autoencoders (Hütel et al. 2018) or nonparametric homomorphic filtering (Sreenivasan et al. 2015). Alternatively, several methods have also been proposed
50 to invert non-linear models of the neuronal and hemodynamic coupling (Riera et al. 2004; Friston et al. 2008; Havlicek et al. 2011; Aslan et al. 2016; Madi and Karameh 2017; Ruiz-Euler et al. 2018).

Among the variety of approaches, those based on regularized least squares estimators have been more employed due to their appropriate performance at small spatial scales (e.g. voxelwise). Rel-

55 event for this work, two different formulations can be established for the regularized least squares problem, either based on a synthesis-based or analysis-based model Elad et al. 2007; Ortelli and van de Geer 2020. The rationale of the synthesis-based model is that we know or suspect that the true signal (here, the neuronally-driven BOLD component of the fMRI signal) can be represented as a linear combination of predefined patterns or dictionary atoms (for instance, the hemodynamic response function). In contrast, the analysis-based approach considers that the true signal is analyzed by some relevant operator and the resulting signal is small (i.e. sparse).

60 This note revisits synthesis- and analysis-based deconvolution methods for fMRI data and comprises four sections. In the first, we present the theory behind two state-of-the-art deconvolution approaches based on regularized least squares estimators that promote sparsity: Paradigm Free
65 Mapping (PFM) (Gaudes et al. 2013) — available in AFNI as *3dPFM* and *3dMEPFM* for single-echo and multi-echo data, respectively — and Total Activation (TA) (Karahanoglu et al. 2013) — available as part of the *iCAPs toolbox*. We then assess their performance controlling for a fair comparison on simulated and experimental data. Finally, we discuss the benefits and shortcomings of each technique and conclude with our vision on potential extensions and developments.

70 2. Theory

2.1. Notations and definitions

Matrices of size N rows and M columns are denoted by boldface capital letters, e.g., $\mathbf{X} \in \mathcal{R}^{N \times M}$, whereas column vectors of length N are denoted as boldface lowercase letters, e.g. $\mathbf{x} \in \mathcal{R}^N$. Scalars are denoted by lowercase letters, e.g., k . Continuous functions are denoted by brackets, e.g., $h(t)$, while discrete functions are denoted by square brackets, e.g., $x[k]$. The euclidean norm of a matrix \mathbf{X} is denoted as $\|\mathbf{X}\|_2$, the ℓ_1 -norm is denoted by $\|\mathbf{X}\|_1$ and the Frobenius norm is denoted by $\|\mathbf{X}\|_F$.

2.2. Conventional general linear model analysis

Conventional general linear model (GLM) analysis puts forward a number of regressors incorporating hypothetical knowledge about the paradigm or behavior. For instance, the timing of epochs for a certain condition can be modeled as an indicator function $p(t)$ (e.g. Dirac functions for event-related designs or box-car functions for block-designs) convolved with the hemodynamic response function (HRF) $h(t)$, and sampled at TR resolution (Friston et al. 1994, 1998; Boynton et al. 1996; Cohen 1997):

$$p(t) \rightarrow p * h(t) \rightarrow x[k] = p * h(k \cdot \text{TR}).$$

The vector $\mathbf{x} = [x[k]]_{k=1,\dots,N} \in \mathcal{R}^N$ then constitutes the regressor modelling the hypothetical response, and several of them can be stacked as columns of the design matrix $\mathbf{X} = [\mathbf{x}_1 \dots \mathbf{x}_L] \in \mathcal{R}^{N \times L}$, leading to the well-known GLM formulation:

$$\mathbf{y} = \mathbf{X}\boldsymbol{\beta} + \mathbf{e}, \quad (1)$$

80 where the empirical timecourse $\mathbf{y} \in \mathcal{R}^N$ is explained by a linear combination of the regressors in \mathbf{X} weighted by the parameters in $\boldsymbol{\beta} \in \mathcal{R}^L$ and corrupted by additive noise $\mathbf{e} \in \mathcal{R}^N$. Under independent and identically distributed Gaussian assumptions of the latter, the maximum likelihood estimate of the parameter weights reverts to the ordinary least-squares estimator; i.e., minimizing the residual sum of squares between the fitted model and measurements. The number of regressors L is typically

much less than the number of measurements N , and thus the regression problem is over-determined
⁸⁵ and does no require additional constraints or assumptions.

In the deconvolution approach, no prior knowledge of the hypothetical response is taken into account, and the purpose is to estimate the deconvolved activity-inducing signal \mathbf{s} from the measurements \mathbf{y} , which can be formulated as the signal model

$$\mathbf{y} = \mathbf{H}\mathbf{s} + \mathbf{e}, \quad (2)$$

where $\mathbf{H} \in \mathcal{N} \times \mathcal{N}$ is a Toeplitz matrix that represents the discrete convolution with the HRF, and $\mathbf{s} \in \mathcal{R}^N$ is a length- N vector with the unknown activity-inducing signal. Note that the temporal resolution of the activiy-inducing signal and the corresponding Toeplitz matrix is generally assumed to be equal to TR of the acquisition, but it could also be higher if an upsampled estimate is desired.
⁹⁰ Despite the apparent similarity with the GLM equation, there are two important differences. First, the multiplication with the design matrix of the GLM is an expansion as a weighted linear combination of its columns, while the multiplication with the HRF matrix represents a convolution operator. Second, determining \mathbf{s} is an ill-posed problem given the nature of the HRF; e.g., as can be seen intuitively, the rows of \mathbf{H} are highly correlated due to large overlap between shifted HRFs (see
⁹⁵ Figure ??B), thus introducing ambiguity and instability in the estimates of \mathbf{s} . Therefore, additional assumptions under the form of regularization are needed.

2.3. Paradigm-free mapping

The first approach for deconvolution is based on the forward model formulation of Eq. (2); i.e., the to-be-recovered activity-inducing signal $\hat{\mathbf{s}}$ is convolved by the HRF and compared against the measured timecourse in the least-squares sense:

$$\hat{\mathbf{s}} = \arg \min_{\mathbf{s}} \frac{1}{2} \|\mathbf{y} - \mathbf{H}\mathbf{s}\|_2^2 + \Omega(\mathbf{s}). \quad (3)$$

The first term quantifies data fitness, which can be justified as the log-likelihood term derived from Gaussian noise assumptions, while the second term $\Omega(\mathbf{s})$ brings in regularization and be interpreted as a prior on the activity-inducing signal. In classical Wiener deconvolution, the (squared) ℓ_2 -norm of \mathbf{s} is imposed (i.e., $\Omega(\mathbf{s}) = \lambda \|\mathbf{s}\|_2^2$), which introduces a trade-off, controlled by the regularization parameter λ , between data fit and “energy” of the solution. In paradigm-free mapping (PFM), the formulation of Eq. (3) was considered equivalently as fitting the measurements using the atoms of a dictionary (columns of \mathbf{H}) with corresponding weights (entries of \mathbf{s}) (Gaudes et al. 2010, 2013; Uruñuela et al. 2020). In addition, sparsity-pursuing regularization was introduced on \mathbf{s} , which in a strict way reverts to choosing $\Omega(\mathbf{s}) = \lambda \|\mathbf{s}\|_0$ and solving the optimization problem (Bruckstein et al. 2009). However, finding the optimal solution to the problem demands an exhaustive search across all possible combinations of the columns of \mathbf{H} . Hence, a pragmatic solution is to solve the convex-relaxed optimization problem for the ℓ_1 -norm, commonly known as the LASSO (Tibshirani 1996):

$$\hat{\mathbf{s}} = \arg \min_{\mathbf{s}} \frac{1}{2} \|\mathbf{y} - \mathbf{H}\mathbf{s}\|_2^2 + \lambda \|\mathbf{s}\|_1, \quad (4)$$

which provides fast convergence to a global solution. From the neuronal perspective, imposing sparsity on the activity-inducing signal expresses that activity, at the fMRI timescale of seconds,
¹⁰⁰ is supposed to be short and typically can be explained by a small number of large entries. Further on, we refer to this assumption as the spike model.

2.4. Total activation

Alternatively, deconvolution can be formulated as a denoising problem where the signal to be recovered is directly fitting the measurements and at the same time satisfying some suitable regularization, which leads to

$$\hat{\mathbf{x}} = \arg \min_{\mathbf{x}} \frac{1}{2} \|\mathbf{y} - \mathbf{x}\|_2^2 + \Omega(\mathbf{x}). \quad (5)$$

Well-known regularized regression techniques such as ridge regression (i.e., $\Omega(\mathbf{x}) = \lambda \|\mathbf{x}\|_2^2$) and elastic net (i.e., $\Omega(\mathbf{x}) = \lambda_1 \|\mathbf{x}\|_2^2 + \lambda_2 \|\mathbf{x}\|_1$) fall under this category [REF]. One other powerful regularizer is total variation (TV), which is the ℓ_1 -norm of the derivative, $\Omega(\mathbf{x}) = \lambda \|\mathbf{Dx}\|_1$, and favors recovery of piecewise-constant signals [REF]. The approach of generalized TV introduces an additional differential operator \mathbf{D}_H in the regularizer that can be tailored as the inverse operator of a linear system (Karahanoglu et al. 2011), that is, $\Omega(\mathbf{x}) = \lambda \|\mathbf{DD}_H \mathbf{x}\|_1$. In the context of hemodynamic deconvolution, total activation is proposed for which the discrete operator \mathbf{D}_H is derived from the inverse of the continuous-domain linearized balloon-windkessel model. Exchanging the poles and zeros of the latter's linear-system characterization leads to a differential operator of the form

$$D_H = \prod_{i=1}^{M_1} (D - \alpha_i I) \left(\prod_{j=1}^{M_2} (D - \gamma_j I) \right)^{-1}, \quad (6)$$

where D is the derivative operator, α_i the zeros, and γ_j the poles. The interested reader is referred to (Karahanoglu et al. 2013) for a detailed description.

Therefore, the solution of the total-activation problem

$$\hat{\mathbf{x}} = \arg \min_{\mathbf{x}} \frac{1}{2} \|\mathbf{y} - \mathbf{x}\|_2^2 + \lambda \|\mathbf{DD}_H \mathbf{x}\|_1 \quad (7)$$

¹⁰⁵ will render the activity-related signal \mathbf{x} for which the activity-inducing signal $\mathbf{s} = \mathbf{D}_H \mathbf{x}$ and so-called innovation signal $\mathbf{u} = \mathbf{Ds}$ will also be available, as they are required for the regularization. We refer to the assumption for the activity-inducing signal as the block model.

2.5. Unifying both perspectives

PFM and TA are based on the synthesis- and analysis-based formulation of the deconvolution problem, respectively. In the first case, the recovered deconvolved signal is synthesized to be matched to the measurements, while in the second case, the recovered signal is directly matched to the measurements but needs to satisfy its analysis in terms of deconvolution. This also corresponds to using the forward or backward model of the hemodynamic system, respectively. Both approaches are equivalent¹ [REF Elad]. First, TA can be made equivalent to PFM by removing the derivative operator of TA's regularizer. It can then be readily verified that replacing in that case $\mathbf{x} = \mathbf{Hs}$ leads to identical equations and thus both assume a spike model. Second, PFM can also be made equivalent to TA, by considering the modified forward model

$$\mathbf{y} = \mathbf{HLu} + \mathbf{e},$$

Would be nice to check a bit closer, this is what I concluded.

¹Without dwelling into technicalities, this equivalence is correct up to the constant, which is in the null space of the derivative operator.

where the activity-inducing signal \mathbf{s} is rewritten in terms of the innovation signal \mathbf{u} ; i.e., the derivative $\mathbf{Ds} = \mathbf{u}$ of \mathbf{s} (Cherkaoui et al. 2019; Uruñuela et al. 2020). This way, PFM will solve for the innovation signal \mathbf{u} :

$$\hat{\mathbf{u}} = \arg \min_{\mathbf{u}} \frac{1}{2} \|\mathbf{y} - \mathbf{H}\mathbf{L}\mathbf{u}\|_2^2 + \lambda \|\mathbf{u}\|_1, \quad (8)$$

and becomes equivalent to TA by replacing $\mathbf{u} = \mathbf{DD}_H \mathbf{x}$, and thus adopting the block model.

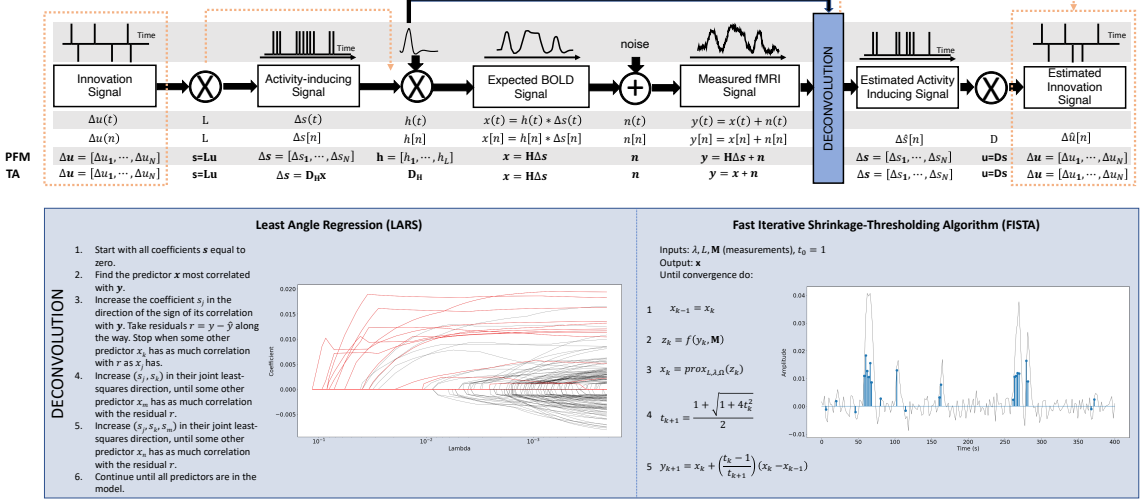


Figure 1: Flowchart detailing the different steps of the fMRI signal and the deconvolution methods described. The orange arrows indicate the flow to estimate the innovation signals. The blue box depicts the two algorithms used in this paper to solve the PFM and TA deconvolution problems.

110 2.6. Algorithms and parameter selection

Despite their algebraic equivalence, both techniques are solved with different techniques. Here, we evaluate PFM and TA solved using least angle regression (LARS) (Efron et al. 2004) and fast iterative shrinkage-thresholding algorithm (FISTA) (Beck and Teboulle 2009), respectively.

In both cases, the correct selection of the regularization parameter λ is a critical decision for the accurate performance of deconvolution methods. Even though many techniques have been proposed in the literature, the optimal strategy that selects λ is yet to be found. For instance, LARS provide all the possible solutions to the optimization problem and their corresponding value of λ , i.e., the regularization path, but do not provide the optimal solution. Therefore, strategies that exploit the regularization path can provide a selection of λ that is close to the optimal. In the case of PFM, the optimal result is given by the Bayesian Information Criterion (BIC) (Schwarz 1978), i.e., the regularization path solution with the minimum BIC is considered an appropriate solution. In the case of TA, the regularization parameter λ is updated on every iteration n , so that the residuals converge to a previously estimated noise level of the data fit $\tilde{\sigma}$. The pre-estimated noise level is calculated from the median absolute deviation (MAD) of fine-scale wavelet coefficients (Daubechies, order 3) (Karahanoğlu et al. 2013):

$$\lambda^{n+1} = \frac{N\tilde{\sigma}}{\frac{1}{2} \|\mathbf{y} - \mathbf{x}^n\|_F^2} \lambda^n, \quad (9)$$

where x^n is the n^{th} iteration estimate, λ^n and λ^{n+1} are the n^{th} and $n+1^{th}$ iteration values for the regularization parameter λ , and N is the number of points in the time-course.

3. Methods

3.1. Simulated data

In order to compare the two methods while controlling for their correct performance, we simulated a 400 seconds (TR = 2 s) activity-inducing signal with five neuronal events, convolved it with the canonical HRF, and we added noise of different sources (physiological, thermal, and motion-related) with different signal-to-noise ratios (SNR = [20 dB, 10 dB, 3 dB]) that represent low, medium and high levels of noise as shown in Figure 2A. Noise was created following the procedure in (Gaudes et al. 2013) as the sum of uncorrelated Gaussian noise and sinusoidal signals to simulate a realistic noise model with thermal noise, cardiac and respiratory physiological fluctuations. We generated the sinusoidal term as

$$\sum_{i=1}^2 \frac{1}{2^{i-1}} (\sin(2\pi f_{r,i}t + \phi_{r,i}) + \sin(2\pi f_{c,i}t + \phi_{c,i})), \quad (10)$$

with up to second-order harmonics per cardiac ($f_{c,i}$) and respiratory ($f_{r,i}$) component that were randomly generated following normal distributions with variance 0.04 and mean if_r and if_c , for $i = [1, 2]$. We set the fundamental frequencies to $f_r = 0.3$ Hz for the respiratory component (?) and $f_c = 1.1$ Hz for the cardiac component (Shmueli et al. 2007). The phases of each harmonic ϕ were randomly selected from a uniform distribution between 0 and 2π radians. In order to simulate physiological noise that is proportional to the change in BOLD signal, a variable ratio between the physiological (σ_P) and the thermal (σ_0) noise was modeled as $\sigma_P/\sigma_0 = a(tSNR)^b + c$, where $a = 5.01 \times 10^{-6}$, $b = 2.81$, and $c = 0.397$. The physiological-thermal noise model was extracted following the experimental measures of the physiological-to-thermal noise ratio at 7T in Table 3 in (Triantafyllou et al. 2005). The code used to simulate the data can be found in the GitHub repository shared in section 6.

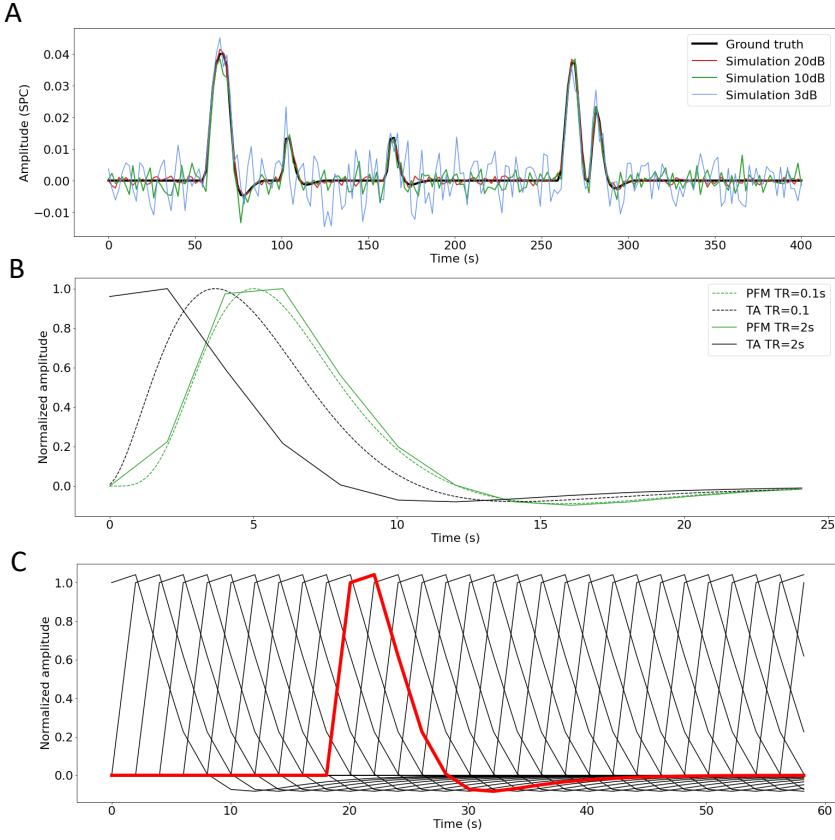


Figure 2: A) Simulated signal with different SNRs (20 dB, 10 dB and 3 dB) and ground truth. B) Canonical HRF models typically used by PFM (green) and TA (black) at TR = 0.1 s (dashed lines) and TR = 2 s (solid lines). Without loss of generality, the waveforms are scaled to unit amplitude for visualization. C) Representation of shifted HRFs at TR = 2 s that build the design matrix for PFM when the HRF model has been matched to that in TA. The red line corresponds to one of the columns of the HRF matrix.

3.2. Experimental data

Motor task dataset: One healthy subject was scanned in a 3T MR scanner (Siemens) as part of a larger experiment under a Basque Center on Cognition, Brain and Language Review Board-approved protocol. T2*-weighted multi-echo fMRI data was acquired with a multiband (MB) multi-echo gradient echo-planar imaging sequence (340 scans, 52 slices, Partial-Fourier = 6/8, voxel size = 2.4x2.4x3 mm³, TR = 1.5 s, TE = 10.6/28.69/46.78/64.87/82.96 ms, multiband factor = 4, flip angle = 70°, GRAPPA = 2).

During the fMRI acquisition, subjects performed a motor task consisting of five different movements (left-hand finger tapping, right-hand finger tapping, moving the left toes, moving the right toes and moving the tongue). These conditions were randomly intermixed every 16 seconds, and were only repeated once the entire set of stimuli were presented. Data preprocessing consisted of optimally combining the echo time datasets, detrending of up to 5th-order Legendre polynomials, spatial smoothing (3 mm FWHM) and normalization to signal percentage change. The onset

and duration of the different conditions can be seen in Figure 5, along with the time-series of a representative voxel in the motor areas corresponding to each of the conditions.

Resting-state datasets: One healthy subject was scanned in a 3T MR scanner (Siemens) as part of a larger experiment under a Basque Center on Cognition, Brain and Language Review Board-approved protocol. Two runs of T2*-weighted fMRI data were acquired during resting-state, each with 10 min duration, with 1) a standard gradient-echo echo-planar imaging sequence (monoband) (TR = 2000 ms, TE = 29 ms, flip-angle = 78°, matrix size = 64x64, voxel size = 3x3x3 mm³, 33 axial slices with interleaved acquisition, slice gap = 0.6 mm) and 2) a simultaneous multislice gradient-echo echo-planar imaging sequence (multiband factor = 3) developed by the Center of Magnetic Resonance Research (University of Minnesota, USA; TR = 800 ms, TE = 29 ms, flip-angle = 60°, matrix size = 64×64, voxel size = 3x3x3 mm³, 42 axial slices with interleaved acquisition, no slice gap). Single-band reference images were also collected in both resting-state acquisitions for head motion realignment. Field maps were also obtained to correct for field distortions.

During both acquisitions, participants were instructed to keep their eyes open, fixating a white cross that they saw through a mirror located on the head coil, and not think about anything specific. The data was pre-processed using AFNI (Cox 1996). First, volumes corresponding to the initial 10 seconds were removed to allow for a steady-state magnetization. Then, the voxel time-series were despiked to reduce large-amplitude deviations and slice-time corrected. Inhomogeneities caused by magnetic susceptibility were corrected with FUGUE (FSL) using the field map images (Jenkinson et al. 2012). Next, functional images were realigned to a base volume (monoband: volume with the lowest head motion; multiband: single-band reference image). Finally, a simultaneous nuisance regression step was performed comprising up to 6th-order Legendre polynomials, low-pass filtering with a cutoff frequency of 0.25 Hz (only on multiband data to match the frequency content of the monoband), 6 realignment parameters plus temporal derivatives, 5 principal components of white matter (WM), 5 principal components of lateral ventricle voxels (anatomical CompCor) and 5 principal components of the brain's edge voxels. WM, CSF and brain's edge-voxel masks were obtained from Freesurfer tissue and brain segmentations. In addition, scans with potential artifacts were identified and censored as the euclidean norm of the temporal derivative of the realignment parameters (ENORM) was larger than 0.4, and the proportion of voxels adjusted in the despiking step exceeded 10%.

3.3. Selection of the hemodynamic response function

By default, PFM and TA make use of different discrete operators to estimate neuronal-related signals: the canonical HRF in the case of PFM, and an HRF resulting from the linear differential operator \mathbf{D}_H in the case of TA. Given the differences between the default selections (see Figure 2B), it is undeniable that one of the two must be adjusted to demonstrate that both methods estimate neuronal-related signals equivalently. Elad et al. 2007 argue that complete equivalence cannot be ensured in the underdetermined case where the number of frames N is lower than the number of voxels V ($N \leq V$), given that the synthesis method (PFM) can only produce results in the column-span of \mathbf{H} , while the analysis approach (TA) does not pose such restriction. Hence, in order to study whether temporal deconvolution of fMRI data can be performed equally with PFM and TA, and to ensure a fair comparison between the two methods, we build the synthesis operator \mathbf{H} with shifted versions of the HRF given by the analysis operator (see Figure 2C) taking advantage of its versatile structure.

185 *3.4. Selection of the regularization parameter*

We use the simulated data to compare the performance of the two deconvolution algorithms with both selection criteria for the regularization parameter λ : a selection based on the BIC solution, and a selection based on the MAD estimate of the noise (see section 2.6). We also evaluate if the algorithms behave differently in terms of the estimation of the activity-inducing signal \hat{s} using the *spike model* in (4) and the innovation signal $\hat{\mathbf{u}}$ using the *block model* in (8).

In order to calculate the regularization paths, we perform LARS with the PFM deconvolution model and obtain the solution for every λ in the regularization path. Then, we use the values of λ obtained with LARS to solve the TA deconvolution model by means of FISTA.

On the other hand, to solve the deconvolution problem with a selection based on the MAD estimate of the noise with PFM, we select the λ corresponding to the residuals that are closest to the estimated noise level of the data $\tilde{\sigma}$. In the case of TA, we apply the temporal regularization in its original form. We do not introduce additional spatial regularization in any of the cases.

195 *3.5. Differences in experimental data*

In order to describe the extent of the discrepancies between the techniques when applied on real fMRI data processing scenarios, we calculate the sum of squares of the differences (SSD) between the estimated activity-inducing signals of PFM and TA on the three experimental datasets as

$$SSD = \frac{\sum_k (\hat{s}_{\text{PFM}}[k] - \hat{s}_{\text{TA}}[k])^2}{N}, \quad (11)$$

where N is the number of frames of the acquisition. The SSD of the innovation signals $\hat{\mathbf{u}}$ was computed equally.

200 At the same time, we evaluate the performance of PFM and TA in comparison with a GLM that takes advantage of the duration and onsets of the stimuli in the motor task data. Given the block design of the motor task, we only make this comparison with the block model.

205 *3.6. Beyond deconvolution*

Finally, we show the usefulness of deconvolution approaches by calculating the co-activation patterns (CAPs) and innovation-driven co-activation patterns (iCAPs) from the obtained activity-inducing and innovation signals. To achieve this, we calculate the average time-series in a seed of 9 voxels located in the precuneus, supramarginal gyrus and occipital gyri independently, and solve the deconvolution problem to find the activity-inducing and innovation signals in the seeds. We then average the maps of time-frames with an amplitude over the 95th percentile threshold and compare the results with the maps obtained by applying the same procedure to the original— i.e., non-deconvolved— signal in the seed.

4. Results

4.1. Performance based on the regularization parameter

215 Figure 3A (left) shows the regularization paths of PFM and TA side by side for the three SNR conditions for the spike model; i.e., the inverse problem described in (4). Each iteration of LARS reduces the value of λ ; i.e., reduces the sparsity promoted by the l_1 -norm, and reveals new non-zero coefficients as shown in the x-axis of the heatmaps. Vertical black lines depict the selection of the regularization parameter based on BIC, and thus, the colored coefficients indicated by the

²²⁰ vertical lines depict the estimated activity-inducing signal $s(t)$. Figure 3A (right) illustrates the resulting estimation of the activity-inducing and neuronal-related signals when basing the selection of λ on BIC for the three simulated SNR conditions. Given that the regularization paths of both techniques are identical, the BIC-based selection of the regularization parameter and the results of deconvolving with said λ are identical too. Thus, Figure 3A demonstrates that, regardless of
²²⁵ the simulated SNR condition, the spike model of both deconvolution algorithms produce identical regularization paths when the same HRF and regularization parameters are applied, and hence, identical estimates of the activity-inducing signal \hat{s} and neuronal-related signal \hat{x} .

The regularization path to estimate innovation signals yields mainly undistinguishable results for both PFM and TA methods as shown in Figure 3A (left). Again, the BIC-based selection of λ is identical for both PFM and TA, and the estimation of the innovation signal u shows no distinguishable differences between the algorithms (see Figure 3A right). Therefore, both PFM and TA yield equivalent regularization paths and estimates of the innovation signal regardless of the simulated SNR condition when applying the same HRF and regularization parameters with the block model.

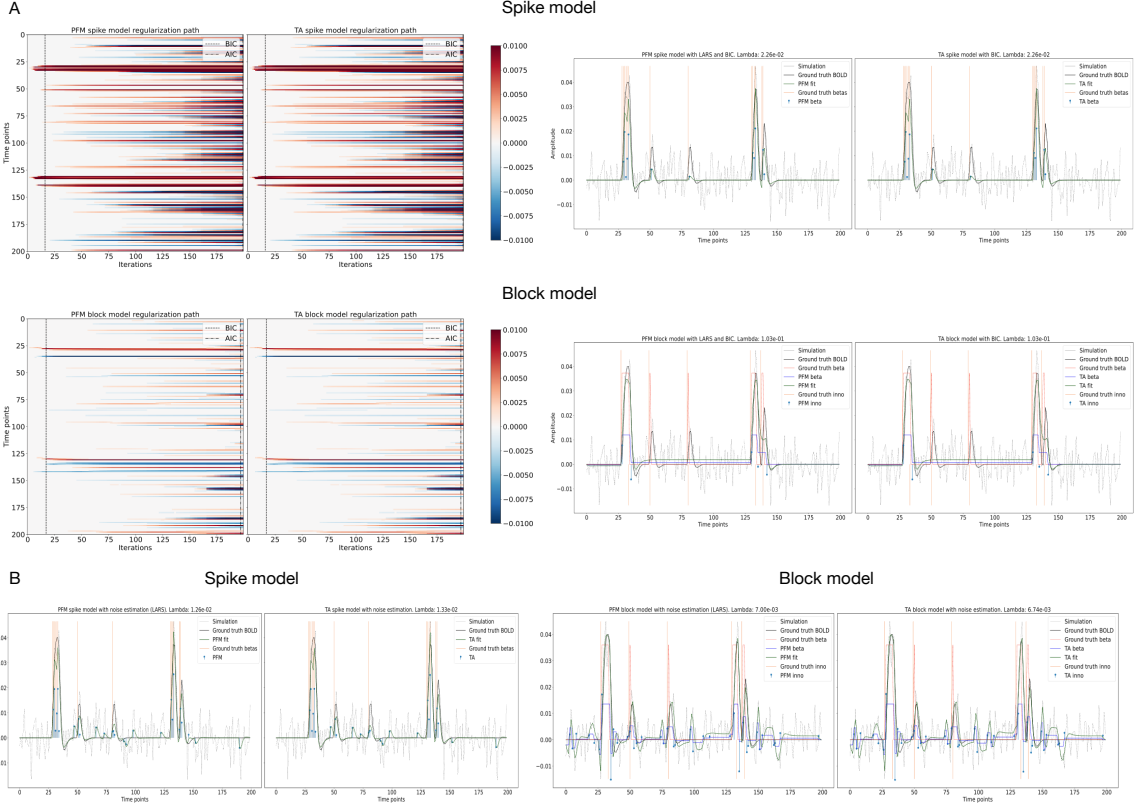


Figure 3: A) (Left) Heatmap of the regularization paths of the activity-inducing (top) and innovation (bottom) signals estimated with PFM and TA as a function of λ for the simulated data with SNR = 3 dB (x-axis: increasing number of iterations or λ as given by LARS; y-axis: time; color: amplitude). Vertical lines denote iterations corresponding to the Akaike and Bayesian Information Criteria (AIC and BIC) optima. (Right) Estimated activity-inducing (blue) and activity-related (green) signals λ is selected based on BIC. B) Estimated activity-inducing, innovation and activity-related (fit, \mathbf{x}) signals when λ is selected based on the MAD method with the spike model (left, with PFM on the left and TA on the right) and block model (right, with PFM on the left and TA on the right) for the simulated data with SNR = 3 dB.

Figure 3B depicts the estimated activity-inducing, innovation, and activity-related signals when updating λ following (9) in the three simulated SNR settings using the spike model (left) and the block model (right). Figure 3B (left) shows nearly identical results between PFM (left) and TA (right) with the use of the spike model. Given that the regularization paths of both techniques are identical, the minimal differences must be the result of slight dissimilarities in the convergence of the residuals to the estimated noise level of the data. Likewise, the use of the block model with a selection of λ based on the MAD estimate of the noise yields results that are identical in practice as shown in Figure 3B (right).

4.2. Performance on experimental data

Figure 4 depicts the SSD of the spike (Figure 4A) and block (Figure 4B) models for the three experimental datasets introduced: motor, monoband and multiband. SSD values are clearly lower

than those of the activity-inducing and innovation signals, suggesting that the differences between PFM and TA are negligible when the spike model (with both selection criteria) and the block model with the BIC selection criteria are employed. A selection of the regularization parameter λ based on the MAD estimate of the noise using the block model produces SSD values that are comparable to those of the innovation signal though. Nevertheless, the largest differences are evident in regions with high vasculature, likely resulting from differences in amplitude of activity-inducing and innovation signals derived from the noisy nature of the fMRI signal in such areas of the brain.

Expand more on interpretation of this Figure.

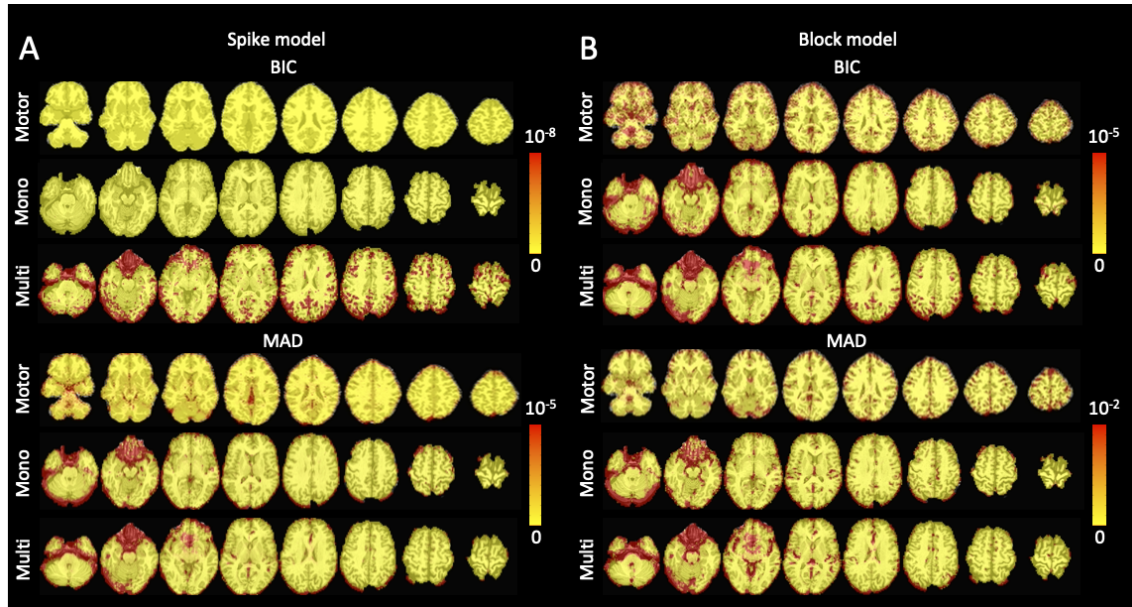


Figure 4: Sum of squares of the differences of the activity-inducing and innovation signals estimated with Paradigm Free Mapping and Total activation for the different selections of the regularization parameter: BIC (top), and MAD (bottom). The sum of square difference maps are shown for the three experimental datasets introduced in Section 3: the motor task (Motor), the monoband resting-state (Mono), and the multiband resting-state (Multi) datasets. A) Sum of squares of the differences when using the spike model. B) Sum of squares of the differences when using the block model.

Figure 5 illustrates the activation time-series, activation maps and PFM-estimated (BIC) activity-related, activity-inducing and innovation signals of a representative voxel in the activated region of each of the conditions for the motor task data. The TA-estimated time-series are not shown because its equivalent performance has already been demonstrated. The activation time-series, calculated as the sum of squares of all voxel amplitudes for a given moment in time, of PFM and TA show nearly identical patterns. Furthermore, the estimated activity-related, activity-inducing and innovation signals clearly reveal the activity patterns of each condition in the task, as they exhibit a BOLD response locked to the onset and duration of the conditions. Overall, activity maps of the innovation signal obtained with PFM and TA highly resemble those obtained with a GLM for individual events. Differences between PFM and TA can be disregarded given their close-to-zero values.

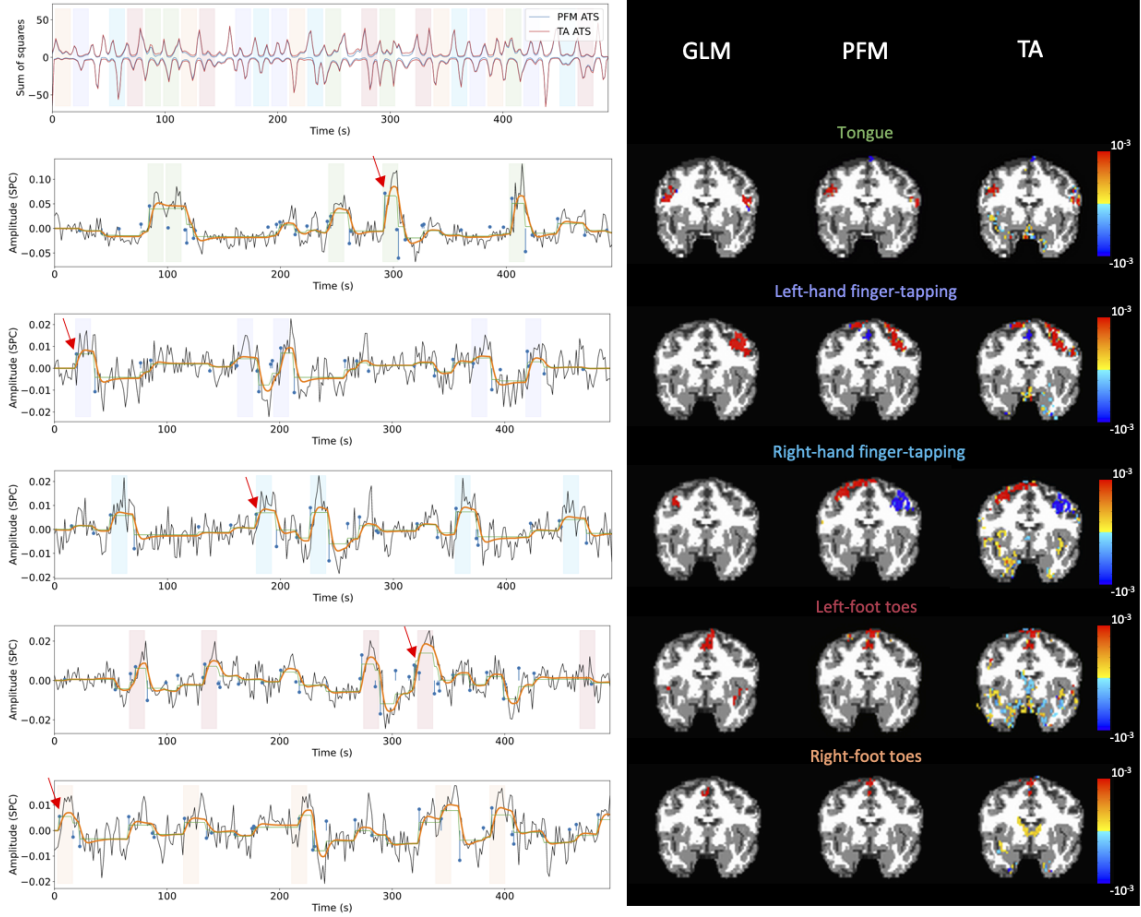


Figure 5: Row 1: Activation time-series of the innovation signals estimated by PFM (in blue) or TA (in red) calculated as the sum of squares at every time-frame. Positive-valued and negative-valued contributions were separated into two distinct time-courses. Color-bands indicate the onset and duration of each condition in the task (green: tongue, purple: left-hand finger-tapping, blue: right-hand finger-tapping, red: left-foot toes, orange: right-foot toes). Rows 2-6: time-series of a representative voxel for each task with the PFM-estimated innovation (blue), PFM-estimated activity-inducing (green), and activity-related (i.e., fitted, orange) signals, with their corresponding GLM, PFM, and TA maps on the right. The maps shown on the right are sampled at the time-point labeled with the red arrows and display the innovation signals at that moment across the whole brain.

4.3. Co-activation patterns

Figure 6 depicts the CAPs and iCAPs obtained from thresholding and averaging the activity-inducing and innovation signals estimated from the multiband data using PFM. Activity maps obtained with the CAPs method show spatial patterns of the default mode network (DMN), dorsal attention network (DAN) and visual network (VIS) that contain less spurious voxels than those obtained from the original data, while maintaining the structure of the networks. On the other hand, spatial patterns acquired with the iCAPs approach, i.e., using the block model, are not as comparable as those obtained with the spike model, suggesting that the spike model is preferable

for this particular dataset.

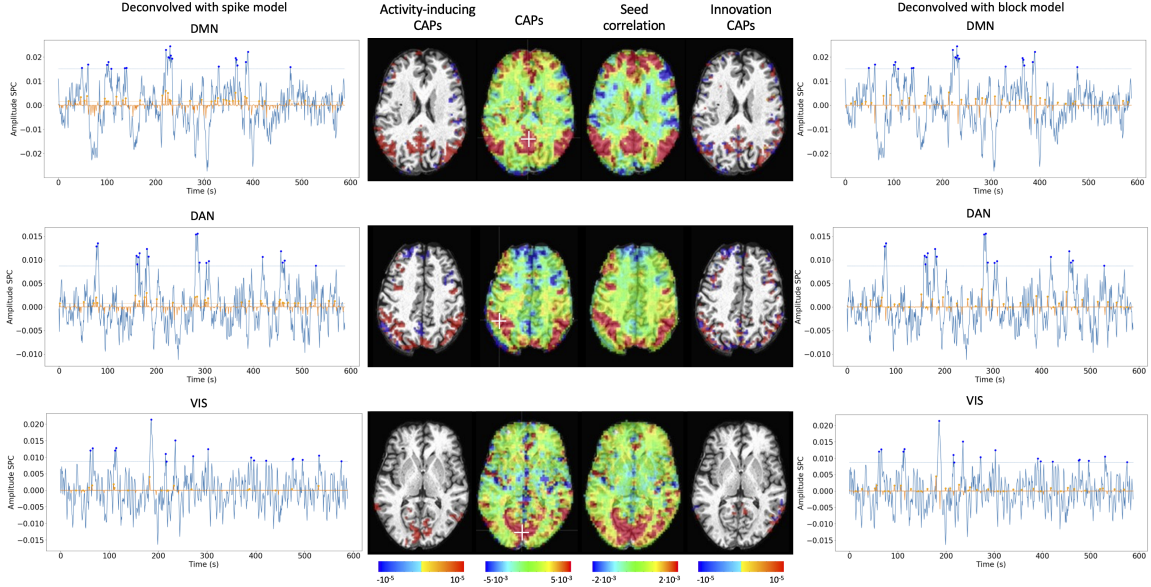


Figure 6: CAPs (left) and iCAPs (right) obtained with the PFM-estimated activity-inducing and innovation signals, respectively. Time-points selected with a 95th percentile threshold are shown over the average time-series (blue) in the seed region (white-cross) and the deconvolved signal (orange). CAPs and iCAPs maps of the seed and deconvolved signals obtained by averaging the selected time-points are illustrated in the center.

What about computation time? Do something similar as Hamza in his PhD?

What about Figs. 6 and 7? Why is PFM and TA not equivalent there?

275 5. Discussion

Folks, I think we need to polish the message for the reader further. If the methods are equivalent, either the reader has learned something about different types of optimization (but this is not yet well described in the paper), or there is a clear practical take-home message.

This work demonstrates that PFM and TA yield practically identical results when the same HRF model and equivalent regularization parameters are employed, demonstrating that synthesis and analysis models are comparable for temporal deconvolution of fMRI data. Hence, we argue that previously observed differences in performance must be due to differences in usage options and the addition of a spatial regularization term by TA. With the equivalence in the temporal deconvolution demonstrated, it is reasonable to assume that additional regularization terms in the spatial or temporal domains would not modify this equivalence when convex operators are employed; e.g., when the regularization problem can be solved by means of the Fast Iterative Shrinkage-Thresholding Algorithm (FISTA) (Beck and Teboulle 2009) or the Generalized Forward-Backward Splitting (Raguet et al. 2013) techniques. Our findings are in line with the equivalence

of analysis and synthesis methods in under-determined cases ($N \leq V$) demonstrated in (Elad et al. 2007) and (Ortelli and van de Geer 2020).

Nevertheless, to achieve optimal performance with any research question in hand, the differences between analysis and synthesis deconvolution methods must be considered. For instance, while TA uses the same HRF to solve both the spike and block models, PFM requires that a modified version of the canonical HRF is used to estimate innovation signals. However, this can be seen as an advantage, since the synthesis operator allows for any HRF shape, only requiring that the coefficients are given on the correct temporal resolution. Given its more intuitive and versatile structure, the synthesis formulation proposed by PFM can easily be extended for the deconvolution of multiple inputs with a common neuronal-related signal, e.g., for the estimation of neuronal-related events on multi-echo data (Caballero-Gaudes et al. 2019).

At the same time, deconvolution techniques can be used to denoise the data prior to the analysis of functional networks as they estimate interactions between brain regions that occur at the neuronal level, which are significantly less affected by noise than hemodynamic interactions (Gitelman et al. 2003). This is of particular interest, as a series of recent studies have attempted to understand neural processes by studying the interactions between BOLD responses without estimating the underlying neuronal activity. For instance, CAPs have been used to replicate seed correlation-based resting-state functional networks with a small portion of the data (Liu and Dux 2013; Liu et al. 2013, 2018; Majeed et al. 2009, 2011; Cifre et al. 2020a,b; Zhang et al. 2020). Likewise, the dynamics of functional connectivity have recently been investigated with the use of co-fluctuations and edge-centric techniques on tasks (Faskowitz et al. 2021), resting-state (Esfahlani et al. 2020) and naturalistic paradigms (Faskowitz et al. 2020; Betzel et al. 2020). Methods based on the multiplication of temporal derivatives have also been presented for the estimation of dynamic functional connectivity on task fMRI data (Shine et al. 2015, 2016). However, the number of studies that take advantage of the potential benefits of using deconvolution methods prior to the analysis of functional connectivity has been scarce.

Finally, taking into account the equivalent performance of analysis and synthesis deconvolution approaches, and the advantages and disadvantages discussed here, it is clear that fMRI deconvolution methods still have room for improvement and their capabilities can be extended to reach a wider community of researchers. For instance, the appropriate formulation for various data acquisition techniques (i.e., single-echo vs multi-echo) could be studied and compared with existing methods (Caballero-Gaudes et al. 2019), or formulations that account for HRF variability could be investigated too (Gaudes et al. 2012; Badillo et al. 2013; Farouj et al. 2019). Furthermore, robust methods to select the regularization parameter (Meinshausen and Bühlmann 2010; Uruñuela et al. 2020) and other potential $\ell_{p,q}$ -norm regularization terms (e.g., $p < 1$) or debiasing approaches could be explored to further improve the accuracy of deconvolution techniques.

6. Code and data availability

The code and materials used in this work can be found in the following GitHub repository: https://github.com/eurunuela/pfm_vs_ta. We encourage the reader to explore the parameters (e.g. SNR, varying HRF options and mismatch between algorithms, TR, number of events, onsets, and durations) in the provided Jupyter notebooks. Likewise, the data used to produce the figures can be found in <https://osf.io/f3ryg/>.

7. Acknowledgements

330 This research was funded by the European Union's Horizon 2020 research and innovation program (agreement No. 713673 of the Marie Skłodowska-Curie grant), La Caixa Foundation (ID 100010434, fellowship code LCF/BQ/IN17/11620063), the Spanish Ministry of Economy and Competitiveness (RYC-2017-21845), the Basque Government (BERC 2018-2021, PIBA_2019_104, PRE_2019_1_005 4), and the Spanish Ministry of Science, Innovation and Universities (PID2019-105520GB-100).

335

References

- Allan, T.W., Francis, S.T., Caballero-Gaudes, C., Morris, P.G., Liddle, E.B., Liddle, P.F., Brookes, M.J., Gowland, P.A., 2015. Functional connectivity in MRI is driven by spontaneous BOLD events. *PLOS ONE* 10, e0124577. doi:10.1371/journal.pone.0124577.
- 340 Aslan, S., Cemgil, A.T., Akin, A., 2016. Joint state and parameter estimation of the hemodynamic model by particle smoother expectation maximization method. *Journal of Neural Engineering* 13, 046010. doi:10.1088/1741-2560/13/4/046010.
- Badillo, S., Vincent, T., Ciuciu, P., 2013. Group-level impacts of within- and between-subject hemodynamic variability in fMRI. *NeuroImage* 82, 433–448. doi:10.1016/j.neuroimage.2013.05.100.
- 345 Beck, A., Teboulle, M., 2009. A fast iterative shrinkage-thresholding algorithm for linear inverse problems. *SIAM Journal on Imaging Sciences* 2, 183–202. doi:10.1137/080716542.
- Betzel, R.F., Byrge, L., Esfahlani, F.Z., Kennedy, D.P., 2020. Temporal fluctuations in the brain's modular architecture during movie-watching. *NeuroImage* 213, 116687. doi:10.1016/j.neuroimage.2020.116687.
- 350 Bolton, T.A., Morgenroth, E., Preti, M.G., Ville, D.V.D., 2020. Tapping into multi-faceted human behavior and psychopathology using fMRI brain dynamics. *Trends in Neurosciences* 43, 667–680. doi:10.1016/j.tins.2020.06.005.
- Bommarito, G., Tarun, A., Farouj, Y., Preti, M.G., Petracca, M., Droby, A., Mendili, M.M.E.,
355 Inglese, M., Ville, D.V.D., 2020. Altered anterior default mode network dynamics in progressive multiple sclerosis. *medRxiv* doi:10.1101/2020.11.26.20238923.
- Boynton, G.M., Engel, S.A., Glover, G.H., Heeger, D.J., 1996. Linear systems analysis of functional magnetic resonance imaging in human v1. *The Journal of Neuroscience* 16, 4207–4221. doi:10.1523/jneurosci.16-13-04207.1996.
- 360 Bruckstein, A.M., Donoho, D.L., Elad, M., 2009. From sparse solutions of systems of equations to sparse modeling of signals and images. *SIAM Review* 51, 34–81. doi:10.1137/060657704.
- Bush, K., Cisler, J., 2013. Decoding neural events from fMRI BOLD signal: A comparison of existing approaches and development of a new algorithm. *Magnetic Resonance Imaging* 31, 976–989. doi:10.1016/j.mri.2013.03.015.

- ³⁶⁵ Bush, K., Zhou, S., Cisler, J., Bian, J., Hazaroglu, O., Gillispie, K., Yoshigoe, K., Kilts, C., 2015. A deconvolution-based approach to identifying large-scale effective connectivity. *Magnetic Resonance Imaging* 33, 1290–1298. doi:10.1016/j.mri.2015.07.015.
- ³⁷⁰ Caballero-Gaudes, C., Moia, S., Panwar, P., Bandettini, P.A., Gonzalez-Castillo, J., 2019. A deconvolution algorithm for multi-echo functional MRI: Multi-echo sparse paradigm free mapping. *NeuroImage* 202, 116081. doi:10.1016/j.neuroimage.2019.116081.
- ³⁷⁵ Cherkaoui, H., Moreau, T., Halimi, A., Ciuciu, P., 2019. Sparsity-based blind deconvolution of neural activation signal in fMRI, in: ICASSP 2019 - 2019 IEEE International Conference on Acoustics, Speech and Signal Processing (ICASSP), IEEE. pp. 1323–1327. doi:10.1109/icassp.2019.8683358.
- ³⁸⁰ Cifre, I., Flores, M.T.M., Ochab, J.K., Chialvo, D.R., 2020a. Revisiting non-linear functional brain co-activations: directed, dynamic and delayed. [arXiv:2007.15728](https://arxiv.org/abs/2007.15728).
- Cifre, I., Zarepour, M., Horovitz, S.G., Cannas, S.A., Chialvo, D.R., 2020b. Further results on why a point process is effective for estimating correlation between brain regions. *Papers in Physics* 12, 120003. doi:10.4279/pip.120003.
- ³⁸⁵ Cohen, M.S., 1997. Parametric analysis of fMRI data using linear systems methods. *NeuroImage* 6, 93–103. doi:10.1006/nimg.1997.0278.
- Costantini, I., Deriche, R., Deslauriers-Gauthier, S., 2021. A paradigm free regularization approach to recover brain activation from functional MRI data. *bioRxiv* doi:10.1101/2021.04.14.438942.
- ³⁹⁰ Cox, R.W., 1996. AFNI: Software for analysis and visualization of functional magnetic resonance neuroimages. *Computers and Biomedical Research* 29, 162–173. doi:10.1006/cbmr.1996.0014.
- Di, X., Biswal, B.B., 2013. Modulatory interactions of resting-state brain functional connectivity. *PLoS ONE* 8, e71163. doi:10.1371/journal.pone.0071163.
- Di, X., Biswal, B.B., 2015. Characterizations of resting-state modulatory interactions in the human brain. *Journal of Neurophysiology* 114, 2785–2796. doi:10.1152/jn.00893.2014.
- ³⁹⁵ Di, X., Biswal, B.B., 2018. Toward task connectomics: Examining whole-brain task modulated connectivity in different task domains. *Cerebral Cortex* 29, 1572–1583. doi:10.1093/cercor/bhy055.
- Efron, B., Hastie, T., Johnstone, I., Tibshirani, R., 2004. Least angle regression. *The Annals of Statistics* 32, 407–499. doi:10.1214/009053604000000067.
- ⁴⁰⁰ Elad, M., Milanfar, P., Rubinstein, R., 2007. Analysis versus synthesis in signal priors. *Inverse Problems* 23, 947–968. doi:10.1088/0266-5611/23/3/007.
- Esfahlani, F.Z., Jo, Y., Faskowitz, J., Byrge, L., Kennedy, D.P., Sporns, O., Betzel, R.F., 2020. High-amplitude cofluctuations in cortical activity drive functional connectivity. *Proceedings of the National Academy of Sciences* 117, 28393–28401. doi:10.1073/pnas.2005531117.
- Farouj, Y., Karahanoglu, F.I., Ville, D.V.D., 2019. Bold signal deconvolution under uncertain hemodynamics: A semi-blind approach, in: 2019 IEEE 16th International Symposium on Biomedical Imaging (ISBI 2019), IEEE. IEEE. pp. 1792–1796. doi:10.1109/isbi.2019.8759248.

- Faskowitz, J., Esfahlani, F.Z., Jo, Y., Sporns, O., Betzel, R.F., 2020. Edge-centric functional network representations of human cerebral cortex reveal overlapping system-level architecture. Technical Report 12. doi:10.1038/s41593-020-00719-y.
- Faskowitz, J., Tanner, J.C., Mišić, B., Betzel, R.F., 2021. An edge-centric model for harmonizing multi-relational network datasets. Preprint. doi:10.1101/2021.01.07.425450.
- Freitas, L.G., Bolton, T.A., Krikler, B.E., Jochaut, D., Giraud, A.L., Hüppi, P.S., Ville, D.V.D., 2020. Time-resolved effective connectivity in task fMRI: Psychophysiological interactions of co-activation patterns. NeuroImage 212, 116635. doi:10.1016/j.neuroimage.2020.116635.
- Friston, K., Fletcher, P., Josephs, O., Holmes, A., Rugg, M., Turner, R., 1998. Event-related fMRI: Characterizing differential responses. NeuroImage 7, 30–40. doi:10.1006/nimg.1997.0306.
- Friston, K., Trujillo-Barreto, N., Daunizeau, J., 2008. DEM: A variational treatment of dynamic systems. NeuroImage 41, 849–885. doi:10.1016/j.neuroimage.2008.02.054.
- Friston, K.J., Jezzard, P., Turner, R., 1994. Analysis of functional MRI time-series. Human Brain Mapping 1, 153–171. doi:10.1002/hbm.460010207.
- Gaudes, C.C., Karahanoglu, F.I., Lazeyras, F., Ville, D.V.D., 2012. Structured sparse deconvolution for paradigm free mapping of functional MRI data, in: 2012 9th IEEE International Symposium on Biomedical Imaging (ISBI), IEEE. IEEE. pp. 322–325. doi:10.1109/isbi.2012.6235549.
- Gaudes, C.C., Petridou, N., Dryden, I.L., Bai, L., Francis, S.T., Gowland, P.A., 2010. Detection and characterization of single-trial fMRI bold responses: Paradigm free mapping. Human Brain Mapping 32, 1400–1418. doi:10.1002/hbm.21116.
- Gaudes, C.C., Petridou, N., Francis, S.T., Dryden, I.L., Gowland, P.A., 2013. Paradigm free mapping with sparse regression automatically detects single-trial functional magnetic resonance imaging blood oxygenation level dependent responses. Human Brain Mapping , n/a–n/adoi:10.1002/hbm.21452.
- Gerchen, M.F., Bernal-Casas, D., Kirsch, P., 2014. Analyzing task-dependent brain network changes by whole-brain psychophysiological interactions: A comparison to conventional analysis. Human Brain Mapping 35, 5071–5082. doi:10.1002/hbm.22532.
- Gitelman, D.R., Penny, W.D., Ashburner, J., Friston, K.J., 2003. Modeling regional and psychophysiological interactions in fMRI: the importance of hemodynamic deconvolution. NeuroImage 19, 200–207. doi:10.1016/s1053-8119(03)00058-2.
- Glover, G.H., 1999. Deconvolution of impulse response in event-related BOLD fMRI1. NeuroImage 9, 416–429. doi:10.1006/nimg.1998.0419.
- Gonzalez-Castillo, J., Caballero-Gaudes, C., Topolski, N., Handwerker, D.A., Pereira, F., Bandettini, P.A., 2019. Imaging the spontaneous flow of thought: Distinct periods of cognition contribute to dynamic functional connectivity during rest. NeuroImage 202, 116129. doi:10.1016/j.neuroimage.2019.116129.
- Havlicek, M., Friston, K.J., Jan, J., Brazdil, M., Calhoun, V.D., 2011. Dynamic modeling of neuronal responses in fMRI using cubature kalman filtering. NeuroImage 56, 2109–2128. doi:10.1016/j.neuroimage.2011.03.005.

- Hernandez-Garcia, L., Ulfarsson, M.O., 2011. Neuronal event detection in fMRI time series using iterative deconvolution techniques. *Magnetic Resonance Imaging* 29, 353–364. doi:10.1016/j.mri.2010.10.012.
- ⁴⁴⁵ Hütel, M., Antonelli, M., Melbourne, A., Ourselin, S., 2021. Hemodynamic matrix factorization for functional magnetic resonance imaging. *NeuroImage* 231, 117814. doi:10.1016/j.neuroimage.2021.117814.
- ⁴⁵⁰ Hütel, M., Melbourne, A., Ourselin, S., 2018. Neural activation estimation in brain networks during task and rest using BOLD-fMRI, in: Medical Image Computing and Computer Assisted Intervention – MICCAI 2018, Springer. Springer International Publishing. pp. 215–222. doi:10.1007/978-3-030-00931-1_25.
- Jenkinson, M., Beckmann, C.F., Behrens, T.E., Woolrich, M.W., Smith, S.M., 2012. FSL. *NeuroImage* 62, 782–790. doi:10.1016/j.neuroimage.2011.09.015.
- ⁴⁵⁵ Karahanoglu, F.I., Bayram, İ., Ville, D.V.D., 2011. A signal processing approach to generalized 1-d total variation. *IEEE Transactions on Signal Processing* 59, 5265–5274. doi:10.1109/tsp.2011.2164399.
- Karahanoğlu, F.I., Caballero-Gaudes, C., Lazeyras, F., Ville, D.V.D., 2013. Total activation: fMRI deconvolution through spatio-temporal regularization. *NeuroImage* 73, 121–134. doi:10.1016/j.neuroimage.2013.01.067.
- ⁴⁶⁰ Karahanoglu, F.I., Grouiller, F., Gaudes, C.C., Seeck, M., Vulliemoz, S., Ville, D.V.D., 2013. Spatial mapping of interictal epileptic discharges in fMRI with total activation, in: 2013 IEEE 10th International Symposium on Biomedical Imaging, Ieee. IEEE. pp. 1500–1503. doi:10.1109/isbi.2013.6556819.
- ⁴⁶⁵ Karahanoglu, F.I., Ville, D.V.D., 2015. Transient brain activity disentangles fMRI resting-state dynamics in terms of spatially and temporally overlapping networks. *Nature Communications* 6, 7751. doi:10.1038/ncomms8751.
- Karahanoğlu, F.I., Ville, D.V.D., 2017. Dynamics of large-scale fMRI networks: Deconstruct brain activity to build better models of brain function. *Current Opinion in Biomedical Engineering* 3, 28–36. doi:10.1016/j.cobme.2017.09.008.
- ⁴⁷⁰ Keilholz, S., Caballero-Gaudes, C., Bandettini, P., Deco, G., Calhoun, V., 2017. Time-resolved resting-state functional magnetic resonance imaging analysis: Current status, challenges, and new directions. *Brain Connectivity* 7, 465–481. doi:10.1089/brain.2017.0543.
- ⁴⁷⁵ Kinany, N., Pirondini, E., Micera, S., Ville, D.V.D., 2020. Dynamic functional connectivity of resting-state spinal cord fMRI reveals fine-grained intrinsic architecture. *Neuron* 108, 424–435.e4. doi:10.1016/j.neuron.2020.07.024.
- Liu, X., Chang, C., Duyn, J.H., 2013. Decomposition of spontaneous brain activity into distinct fMRI co-activation patterns. *Frontiers in Systems Neuroscience* 7, 101. doi:10.3389/fnsys.2013.00101.

- Liu, X., Duyn, J.H., 2013. Time-varying functional network information extracted from brief
 480 instances of spontaneous brain activity. *Proceedings of the National Academy of Sciences* 110,
 4392–4397. doi:10.1073/pnas.1216856110.
- Liu, X., Zhang, N., Chang, C., Duyn, J.H., 2018. Co-activation patterns in resting-state fMRI
 signals. *NeuroImage* 180, 485–494. doi:10.1016/j.neuroimage.2018.01.041.
- Lopes, R., Lina, J., Fahoum, F., Gotman, J., 2012. Detection of epileptic activity in fMRI without
 485 recording the EEG. *NeuroImage* 60, 1867–1879. doi:10.1016/j.neuroimage.2011.12.083.
- Loula, J., Varoquaux, G., Thirion, B., 2018. Decoding fMRI activity in the time domain improves
 classification performance. *NeuroImage* 180, 203–210. doi:10.1016/j.neuroimage.2017.08.018.
- Lurie, D.J., Kessler, D., Bassett, D.S., Betzel, R.F., Breakspear, M., Kheilholz, S., Kucyi, A.,
 490 Liégeois, R., Lindquist, M.A., McIntosh, A.R., Poldrack, R.A., Shine, J.M., Thompson, W.H.,
 Bielczyk, N.Z., Douw, L., Kraft, D., Miller, R.L., Muthuraman, M., Pasquini, L., Razi, A.,
 Vidaurre, D., Xie, H., Calhoun, V.D., 2020. Questions and controversies in the study of time-
 varying functional connectivity in resting fMRI. *Network Neuroscience* 4, 30–69. doi:10.1162/
 netn_a_00116.
- Madi, M.K., Karameh, F.N., 2017. Hybrid cubature kalman filtering for identifying nonlinear
 495 models from sampled recording: Estimation of neuronal dynamics. *PLOS ONE* 12, e0181513.
 doi:10.1371/journal.pone.0181513.
- Majeed, W., Magnuson, M., Hasenkamp, W., Schwab, H., Schumacher, E.H., Barsalou, L., Keil-
 holz, S.D., 2011. Spatiotemporal dynamics of low frequency BOLD fluctuations in rats and
 humans. *NeuroImage* 54, 1140–1150. doi:10.1016/j.neuroimage.2010.08.030.
- 500 Majeed, W., Magnuson, M., Keilholz, S.D., 2009. Spatiotemporal dynamics of low frequency
 fluctuations in BOLD fMRI of the rat. *Journal of Magnetic Resonance Imaging* 30, 384–393.
 doi:10.1002/jmri.21848.
- Meinshausen, N., Bühlmann, P., 2010. Stability selection. *Journal of the Royal Statistical Society:
 Series B (Statistical Methodology)* 72, 417–473. doi:10.1111/j.1467-9868.2010.00740.x.
- 505 Ortelli, F., van de Geer, S., 2020. Oracle inequalities for square root analysis estimators with
 application to total variation penalties. *Information and Inference: A Journal of the IMA* doi:10.1093/imaiia/iaaa002.
- Petridou, N., Gaudes, C.C., Dryden, I.L., Francis, S.T., Gowland, P.A., 2012. Periods of rest in
 510 fMRI contain individual spontaneous events which are related to slowly fluctuating spontaneous
 activity. *Human Brain Mapping* 34, 1319–1329. doi:10.1002/hbm.21513.
- Pidnebesna, A., Fajnerová, I., Horáček, J., Hlinka, J., 2019. Estimating sparse neuronal signal from
 hemodynamic response: the mixture components inference approach. *bioRxiv* doi:10.1101/2019.
 12.19.876508.
- 515 Preti, M.G., Bolton, T.A., Ville, D.V.D., 2017. The dynamic functional connectome: State-of-the-
 art and perspectives. *NeuroImage* 160, 41–54. doi:10.1016/j.neuroimage.2016.12.061.

- Raguet, H., Fadili, J., Peyré, G., 2013. A generalized forward-backward splitting. *SIAM Journal on Imaging Sciences* 6, 1199–1226. doi:10.1137/120872802.
- Riera, J.J., Watanabe, J., Kazuki, I., Naoki, M., Aubert, E., Ozaki, T., Kawashima, R., 2004. A state-space model of the hemodynamic approach: nonlinear filtering of BOLD signals. *NeuroImage* 21, 547–567. doi:10.1016/j.neuroimage.2003.09.052.
- Ruiz-Euler, H.C., Marques, J.R.F., Kappen, H.J., 2018. Nonlinear deconvolution by sampling biophysically plausible hemodynamic models. [arXiv:1803.08797](https://arxiv.org/abs/1803.08797).
- Schwarz, G., 1978. Estimating the dimension of a model. *The Annals of Statistics* 6, 461–464. doi:10.1214/aos/1176344136.
- Shine, J.M., Bissett, P.G., Bell, P.T., Koyejo, O., Balsters, J.H., Gorgolewski, K.J., Moodie, C.A., Poldrack, R.A., 2016. The dynamics of functional brain networks: Integrated network states during cognitive task performance. *Neuron* 92, 544–554. doi:10.1016/j.neuron.2016.09.018.
- Shine, J.M., Koyejo, O., Bell, P.T., Gorgolewski, K.J., Gilat, M., Poldrack, R.A., 2015. Estimation of dynamic functional connectivity using multiplication of temporal derivatives. *NeuroImage* 122, 399–407. doi:10.1016/j.neuroimage.2015.07.064.
- Shmueli, K., van Gelderen, P., de Zwart, J.A., Horovitz, S.G., Fukunaga, M., Jansma, J.M., Duyn, J.H., 2007. Low-frequency fluctuations in the cardiac rate as a source of variance in the resting-state fMRI BOLD signal. *NeuroImage* 38, 306–320. doi:10.1016/j.neuroimage.2007.07.037.
- Sreenivasan, K.R., Havlicek, M., Deshpande, G., 2015. Nonparametric hemodynamic deconvolution of fMRI using homomorphic filtering. *IEEE Transactions on Medical Imaging* 34, 1155–1163. doi:10.1109/tmi.2014.2379914.
- Tarun, A., Wainstein-Andriano, D., Sterpenich, V., Bayer, L., Perogamvros, L., Solms, M., Ax-macher, N., Schwartz, S., Ville, D.V.D., 2020. NREM sleep stages specifically alter dynamical integration of large-scale brain networks. *Iscience* 24, 101923. doi:10.1101/2020.07.08.193508.
- Tibshirani, R., 1996. Regression shrinkage and selection via the lasso. *Journal of the Royal Statistical Society: Series B (Methodological)* 58, 267–288. doi:10.1111/j.2517-6161.1996.tb02080.x.
- Triantafyllou, C., Hoge, R., Krueger, G., Wiggins, C., Potthast, A., Wiggins, G., Wald, L., 2005. Comparison of physiological noise at 1.5 t, 3 t and 7 t and optimization of fMRI acquisition parameters. *NeuroImage* 26, 243–250. doi:10.1016/j.neuroimage.2005.01.007.
- Uruñuela, E., Jones, S., Crawford, A., Shin, W., Oh, S., Lowe, M., Caballero-Gaudes, C., 2020. Stability-based sparse paradigm free mapping algorithm for deconvolution of functional MRI data. *Proceedings of the Annual International Conference of the IEEE Engineering in Medicine and Biology Society*, EMBS 2020-July, 1092–1095. doi:10.1109/embc44109.2020.9176137.
- Zhang, X., Pan, W.J., Keilholz, S.D., 2020. The relationship between BOLD and neural activity arises from temporally sparse events. *NeuroImage* 207, 116390. doi:10.1016/j.neuroimage.2019.116390.
- Zöller, D., Sandini, C., Karahanoğlu, F.I., Padula, M.C., Schaer, M., Eliez, S., Ville, D.V.D., 2019. Large-scale brain network dynamics provide a measure of psychosis and anxiety in 22q11.2 deletion syndrome. *Biological Psychiatry: Cognitive Neuroscience and Neuroimaging* 4, 881–892. doi:10.1101/551796.